Dispersion Engineering for Advanced Temporal Imaging Modalities

Xin Dong†, Sheng Wang†, Minghui Shi, Bowen Li, Liao Chen, Chi Zhang, and Kenneth K. Y. Wong

***Abstract*—Temporal imaging provides a promising platform for ultrafast signal processing in both spectral and temporal domains. Most temporal imaging systems consist of time-lens and temporal dispersion; while optical fibers are desirable to achieve the dispersion component by virtue of their acceptable losses. On the other hand, parametric mixing-based time-lens is commonly used in temporal imaging thanks to the high modulation depth. In those situations, highly nonlinear fiber (HNLF) is used as the nonlinear medium. However, third-order dispersion (TOD) exists in commercial fibers will incur temporal aberration on the system. For instance, the inherent dispersion in HNLF decreases the conversion bandwidth of the parametric process, which restricts the performance of time-lens. In this article, we present our recent efforts in dispersion engineering for temporal imaging systems, both in the temporal dispersion and the nonlinear medium. All these efforts could inspire more innovative applications of temporal imaging modalities in the future.**

***Index Terms*—Dispersion, temporal imaging, parametric mixing, space–time duality, spectrum analysis, ultrafast imaging, ultrafast measurement.**

I. Introduction

Single-shot spectral and temporal waveform characterization have been increasingly demanding in various fields including optical dynamics observation [1]-[3], chemical and biological analysis [4], [5], and medical diagnosis [6], [7]. Resolving those processes in ultra-short time scales with MHz frame rate would not only benefit better perception of our surrounding environment but also facilitate the understanding of the intrinsic mechanisms and principles such as the formation of soliton explosion or collision [8]-[11]. However, such a conception has an inherent gap with the current detection instruments. Owing to the lack of high-performance devices, based on space-time duality [12]-[14], temporal imaging technique [15]-[17] has been proposed and developed constantly to process the signal such as time magnifier and parametric spectro-temporal analyzer (PASTA) [46], [47].

Similar to spatial imaging system, temporal imaging system relies on time-lens [12], which imparts the temporal quadratic phase modulation on input signal. The most direct way to achieve phase modulation through phase modulator (PM) while the maximum phase shift is limited [14]. Cross-phase modulation (XPM) can also be applied to achieve a larger phase shift. However, the phase shift of XPM depends on the pump power [16], [17]. Thus, high power is required to achieve high modulation depth, which will result in self-phase modulation (SPM) and distorts the original intensity envelope. Compared with the above two methods, parametric mixing is commonly used in temporal imaging systems by virtue of the high modulation depth. Fig. 1 demonstrates the mechanism of a typical time-lens system based on four-wave mixing (FWM) [18], [19]. Utilizing the temporal far-field diffraction induced by temporal dispersion, the original pump pulse evolved into chirp pulse with quadratic phase information which can be further imparted on the signal with parametric mixing process. In this scheme, there are two key parts, dispersion and nonlinear medium, which determine the performance of time-lens.

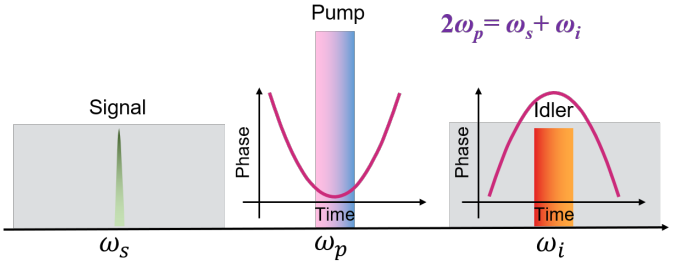

Fig. 1. Schematic diagram of time-lens system utilizing four-wave mixing.

To achieve temporal far-field diffraction, the pump pulse passes through a dispersion medium with large temporal dispersion. Thanks to the development of optical fiber communication systems, optical fibers can achieve both normal dispersion and anomalous dispersion with an ultra-low loss (e.g., 0.14 dB/km) [20]. Besides, optical fibers can be

Manuscript Submitted November 29, 2022. This work was supported in part by the Research Grants Council of the HKSAR, China under Projects HKU 17210522, HKU C7074-21G, HKU 17205321, HKU 17200219, HKU 17209018, CityU T42-103/16-N and Health@InnoHK program of the Innovation and Technology Commission of the Hong Kong SAR Government. (†These authors contributed equally to this work. Corresponding author: Kenneth K. Y. Wong and Chi Zhang.)

X. Dong, M. Shi, and K. K. Y. Wong are with the Photonic Systems Research Laboratory, Department of Electrical and Electronic Engineering, University of Hong Kong, Hong Kong (e-mail: dongxin@connect.hku.hk; shengg@connect.hku.hk; shimh@connect.hku.hk; kywong@eee.hku.hk). S. Wang is with the School of Instrument Science and Optoelectronics Engineering, Hefei University of Technology, Anhui, Hefei, China. K. K. Y. Wong is also with Advanced Biomedical Instrumentation Centre, Hong Kong Science Park, Shatin, New Territories, Hong Kong.

B. Li is with the Key Laboratory of Optical Fiber Sensing and Communications, University of Electronic Science and Technology of China (email: bowen.li@uestc.edu.cn).

L. Chen and C. Zhang are with the Wuhan National Laboratory for Optoelectronics, Huazhong University of Science and Technology, Wuhan 430074, China (e-mail: liaochenchina@hust.edu.cn; chizheung@hust.edu.cn).

conveniently obtained because of the mature market for optical fiber communication systems. As a result, fibers become the ideal medium to achieve large temporal dispersion. Ideally, with the dispersion introduced by fibers, the pump pulse will evolve into the linear chirp pulse with the pure quadratic phase information, which is caused by the group velocity dispersion (GVD) of the dispersion medium. However, high-order dispersion in the fiber, especially third-order dispersion (TOD) will lead to distortion of the quadratic phase information, causing temporal aberrations in temporal imaging systems [12], [13]. Although there are fibers designed to achieve minimum TOD, those fibers are not commercially available because of the complex design and fabrication process [48]. Some other components, e.g., free-space angular-chirp-enhanced delay (FACED) and chirped fiber Bragg grating (CFBG) can provide dispersion without TOD [21]. However, there are ripples [29] in dispersion, which will also lead to the distortion of ideal quadratic phase information. Inspired by the dispersion compensation of optical communication systems [22], we developed two dispersion engineering methods to eliminate TOD recently, including the combination of two types of fibers and the optical phase conjunction (OPC)-based method. Furthermore, for a complete temporal imaging system, dispersion is also indispensable in the other parts, e.g., the input dispersion and the output dispersion. The existence of high-order dispersion also introduces temporal aberration [12], which is similar to geometric aberration in spatial imaging systems.

On the other hand, the design of the nonlinear medium is also important for parametric mixing-based temporal imaging systems because the parametric process determines the performance of phase modulation. Firstly, the observation bandwidth is limited by the parametric-mixing conversion bandwidth, which is determined by the phase-matching condition. To obtain a large conversion bandwidth, the minimum accumulated dispersion (mainly consisting of second-order dispersion) of the medium is required. Secondly, the maximum phase shift is determined by the effective pump bandwidth. Because the chirp pulse is used as the pump of parametric mixing, the dispersive walk-off effect between the pump and the signal will increase the total phase mismatch and decrease the effective pump bandwidth. Unlike the phase mismatch due to dispersion, which depends only on even dispersion orders, the walk-off additionally depends on the odd ones. Therefore, the converted pump bandwidth is subject to the TOD of the nonlinear medium. Most conventional highly nonlinear fibers (HNLFs) tend to exhibit large higher-order dispersion (e.g., $\beta_3 = -5.78 \times 10^{-2}$ ps^3/km) [24], so it is difficult to achieve a large converted pump bandwidth for the parametric-mixing process. A dispersion-flattened HNLF achieved a low β_3 (e.g., -3.22×10^{-3} ps^3/km) [25] while also suffering from a zero-dispersion wavelength fluctuation along the fiber [26], [27]. In addition, it has been reported that a parametric mixing time-lens based on nonlinear optical crystal can achieve a converted pump bandwidth up to 40 nm [28], while it requires high power and degrades detection sensitivity. To relax these limitations, we proposed and demonstrated a dispersion-engineered waveguide with low accumulated dispersion and TOD.

In this paper, we review our recent research efforts in dispersion engineering for temporal imaging systems and its applications. In Section II, the principle of operation of the dispersion engineering method will be briefly discussed. In Section III, the modified temporal imaging system with dispersion engineering method will be presented in detail, including the designed waveguide to achieve large parametric process conversion bandwidth, the improved PASTA system with finer resolution and larger observation bandwidth, and an aberration-free time magnifier. In Section IV, the application of dispersion engineering methods will be described, which shows that this method can not only improve the performance of conventional temporal applications, e.g., time-magnifier, time-stretch microscopy, and time-domain OCT, but can also be applied to novel applications, including terahertz spectrum analyzer and ultrafast swept source. Finally, it is a conclusion of our dispersion engineering method for temporal imaging systems.

II. Principle Of Operation

According to the space-time duality, the temporal imaging system follows similar principles to the spatial imaging system, the narrow pulse in the medium with large dispersion will show analogous characteristics to a monochromatic beam in the spatial domain. In most cases, the spatial imaging can be analyzed with the paraxial approximation condition, which can simplify the theoretical model. However, the nonparaxial beam cannot satisfy this condition, resulting in the geometric aberration in spatial imaging systems. Similarly, the narrow-band dispersion approximation condition is also applied in temporal imaging systems. This condition ignores the high-order dispersion, which plays an insignificant role when the optical bandwidth is narrow. Nevertheless, the temporal imaging system seeks to achieve finer resolution, which can only be achieved with large optical bandwidth. Thus, temporal aberration must be considered, and the high-order dispersion should be properly handled in an advanced temporal imaging system. As the common dispersion medium in temporal imaging systems, the frequency-domain transfer function of fiber can be expressed as below [45]:

$$G(\omega) = \exp\left(-\frac{\mathrm{i}\beta_2 L\omega^2}{2} - \frac{\mathrm{i}\beta_3 L\omega^3}{6} - \frac{\mathrm{i}\beta_4 L\omega^4}{24} - \ldots \right) \quad (1)$$

where β_n is the *n-th* order dispersion coefficient. Only β_2 is considered in narrow-band approximation condition, which can be used to generate quadratic phase distribution for a pump pulse in parametric-mixing-based time-lens. However, the higher-order part will result in distortion in quadratic phase modulation, which is similar to the geometric aberration in space optics, as is shown in Fig. 2. Among the high-order dispersion, TOD caused by β_3 plays the most obvious role, thus, two methods are developed to eliminate TOD.

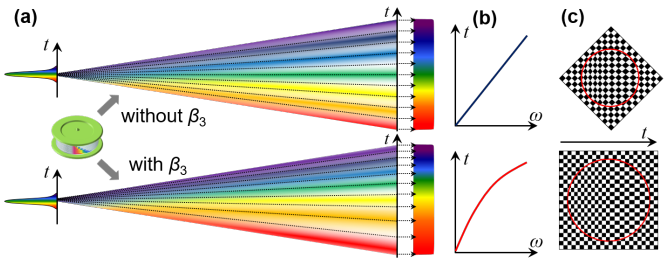

Fig. 2. Conceptual idea of temporal aberration. (a) Third-order dispersion introduced temporal distortion, compared with the quasi-linear β_2 with large temporal dispersion, and resulted in the nonlinear frequency-to-time mapping in (b). (c) Reconstructed two-dimensional temporal aberration, only the horizontal temporal axis is distorted. Copyright 2021, IEEE Xplore [54].

On the other part, the performance of time-lens is also influenced by the parametric process, which occurs in the nonlinear medium. Firstly, the observation bandwidth is actually the conversion bandwidth of the nonlinear medium, which is determined by the phase-matching condition. Generally, the total phase mismatch in time-lens applications can be shown below.

$$\Phi = \beta_{2,medium}\Delta\omega^2 L_{medium} \tag{2}$$

where $\beta_{2,\,medium}$ is the second order dispersion coefficient of the nonlinear medium, and L_{medium} is the length. To meet the phase match condition, the conversion bandwidth $\Delta\omega$ is limited by:

$$\Delta\omega < \sqrt{\frac{1}{\left|\beta_{2,medium}L_{medium}\right|}} \tag{3}$$

Obviously, large conversion bandwidth ($\Delta\omega$) can only be achieved when the GVD ($|\beta_{2,\,medium}\,L_{medium}|$) is small. It is noticed that the pump of the parametric process is the broadened pulse. As mentioned above, large pump bandwidth, which works as the numerical aperture (NA), is required in advanced temporal imaging systems to achieve fine resolution. For the swept chirped pump, the walk-off affects the FWM process and it is typically dominated by TOD in nonlinear medium ($\beta_{3,\,medium}$) for a fixed fiber length L_{medium}. Hence, this condition imposes an additional limitation on the converted pump bandwidth $\Delta\omega_p$ due to TOD in the nonlinear medium given by:

$$\frac{1}{2}\beta_3\left(\omega_s-\omega_p\right)^2\Delta\omega_p L_{medium} < 1 \tag{4}$$

Because of the existence of TOD in nonlinear medium, the bandwidth of the pump is limited, which means the effective phase modulation depth will be decreased. Meanwhile, as the conversion bandwidth increases, the detuning frequency between signal and pump ($\omega_s - \omega_p$) increases, resulting in the decrease of effective pump bandwidth. In conclusion, both $\beta_{2,\,medium}$ and $\beta_{3,\,medium}$ should be optimized to the minimum to achieve large conversion bandwidth and effective pump bandwidth for time-lens.

In conclusion, the advanced temporal imaging system requires dispersion engineering methods both in the dispersion medium and nonlinear medium. In the next part of this section, we will describe the basic principle to optimize the temporal dispersion for temporal imaging systems.

A. TOD elimination by cascading two types of fibers

In optical communication systems, dispersion-compensating fiber (DCF) [49] is used to compensate for the dispersion introduced by single-mode fiber (SMF) because both their GVD (β_2) and TOD (β_3) are opposite. Besides, the ratio between GVD and TOD of SMF is close to the ratio of SMF, which means the TOD and GVD can be generally compensated at the same time. As Fig. 3 shows, the β_3 of large-effective-area fiber (LEAF) is close to DCF while the GVD is negligible, it can be combined with DCF to eliminate the TOD while keeping the most GVD of DCF. The transfer function (ignore higher-order dispersion) of the combination of DCF and LEAF can be expressed as below.

$$G(\omega) = \exp\left[-\frac{i(\beta_{2DCF}L_{DCF}+\beta_{2LEAF}L_{LEAF})\omega^2}{2} - \frac{i(\beta_{3DCF}L_{DCF}+\beta_{3LEAF}L_{LEAF})\omega^3}{6}\right] \tag{5}$$

where β_{2DCF}, β_{3DCF}, β_{2LEAF}, and β_{3LEAF} are the second-order coefficient and third-order dispersion respectively, while L_{DCF} and L_{LEAF} are their lengths. With a proper ratio between L_{DCF} and L_{LEAF}, $\beta_{3DCF}L_{DCF} + \beta_{3LEAF}L_{LEAF}$ can be minimum, which means that the total TOD of the system is eliminated. As Fig. 3 shows, the GVD of DCF and LEAF is opposite and cascading LEAF and DCF will lead to the sacrifice of GVD. Moreover, since β_{3DCF} is about seven times as large as β_{3LEAF}, a seven-fold length of LEAF is required to eliminate TOD of DCF, which will further consume the desired GVD. As a result, the combination of LEAF and DCF is no longer feasible when the desired GVD is large. For instance, more than 100-km LEAF is required to compensate for TOD when the desired GVD is –1.689 ns/nm. To relax this limitation, dispersion-shifted fiber (DSF) is leveraged to compensate TOD of DCF while accumulating GVD since their sign of β_2 is the same and the sign of β_3 is opposite.

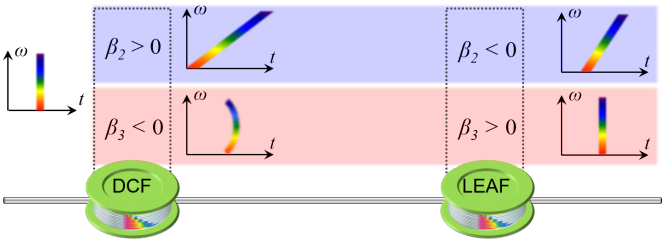

Fig. 3. Third-order dispersion elimination by fiber combination. Precisely length control between DCF and LEAF can fully eliminate the third-order dispersion and remain the second-order dispersion.

B. TOD elimination with temporal phase conjunction

Although cascading two types of fibers is a direct way to eliminate TOD, there is still a limitation. Currently, this method can only be applied to compensate for the TOD of DCF, thus, it can only achieve negative dispersion while both positive and negative dispersion are essential to realize temporal imaging systems. To relax these two limitations, OPC is introduced. The temporal complex conjugation [50] can result in frequency complex conjugation with variable changes in sign, namely, the equivalent frequency-domain transfer function $G(\omega)$ is changed to $G^*(\omega)$, where the asterisk represents complex conjugation. After the OPC process, the even-order dispersion coefficients

(e.g., β_2, β_4) reverse their signs, while the signs of odd-order dispersion coefficients (e.g., β_4) remain the same. As we know, OPC-based dispersion engineering method has been applied to compensate for second-order dispersion in optical fiber communication systems with identical SMFs placed before and after the OPC. But in temporal-imaging applications, large pure temporal dispersion is required [14]. Thus, it is required to be configured in a different way, with the combination of SMF and DCF instead. The total transfer function in frequency domain can be expressed as (ignore higher-order dispersion):

$$G(\omega)=\exp\left[-\frac{i(\beta_{2DCF}L_{DCF}+\beta_{2SMF}L_{SMF})\omega^2}{2}-\frac{i(\beta_{3DCF}L_{DCF}+\beta_{3SMF}L_{SMF})\omega^3}{6}\right] \quad (6)$$

Since both the second and third order dispersion in DCF are opposite to SMF, after the OPC process, the actual signs of β_2 become the same while the signs of β_3 remain the opposite as shown in Fig. 4. As a result, this OPC scheme provide a way to accumulate GVD while eliminating TOD. Furthermore, the sign of GVD can also be easily reversed by exchanging the positions of SMF and DCF.

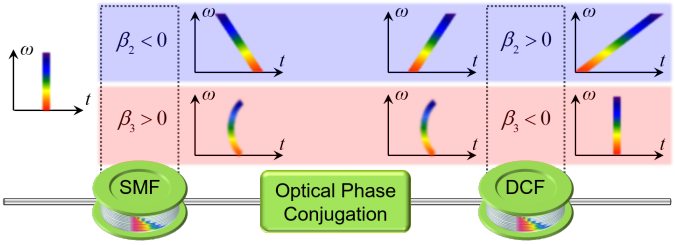

Fig. 4. The effect of optical phase conjugation to β_2 and β_3 respectively, and β_2 with opposite values are accumulated while opposite β_3 is eliminated. Precise length control between SMF and DCF can fully eliminate the third-order dispersion introduced quadratic temporal delay. Copyright 2021, IEEE Xplore [54].

C. *Dispersion engineering for high-nonlinear waveguide*

For the pulsed-pump parametric mixing, a large conversion bandwidth is highly dependent on a low dispersion, while waveguides with a relatively low dispersion slope is potentially more suitable for large converted pump bandwidth applications. Figure 5 shows a schematic diagram of the cross-sectional layout of the silicon waveguide. The device has a silicon-on-insulator structure, with the silicon waveguide placed on a SiO_2 substrate. The silicon waveguide (n = 3.4) surrounded by SiO_2 insulator cladding (n = 1.5) [30] effectively enhances the field confinement in the waveguide, and it can minimize the effective mode area and results in a strong nonlinear parameter [31]. The top-view of the 9-mm-long silicon waveguide is shown in the inset of Fig. 5(a), and it has a cross-section of 600 nm × 220 nm. The measured total insertion loss is about 13 dB, which consists of 4.5-dB/facet grating coupling losses and a 4-dB/cm propagation loss. In contrast, silicon has a large normal material dispersion at the 1550-nm communication wavelength band. To reduce the total GVD, a suitable anomalous waveguide dispersion is achieved by engineering the dimensions of the silicon waveguide. The simulated GVD as a function of wavelength is shown in Fig. 5(b) with different waveguide widths ranging from 400 to 650 nm. Meanwhile, to achieve a larger nondegraded FWM conversion bandwidth for the wideband chirp pump, the silicon waveguide must be carefully designed to reduce its β_3 across the C band. From the simulations, we determine the ideal waveguide width to be about 600 nm for a near-zero GVD point close to 1550 nm. It is clear that tuning the width of the waveguide by 50 nm can shift the dispersion by more than 300 ps/nm/km. Furthermore, the dispersion slope of the silicon waveguides has been reduced to $\beta_3 = -4.25 \times 10^{-3}$ ps^3/km in order to ensure a near-zero GVD for a larger bandwidth at about 1550 nm. As a result, the silicon waveguides have the potential advantage of achieving the relaxed phase-matching condition for the parametric process compared to the HNLF. The comparison results are shown in Fig. 6, where the waveguide demonstrates a more consistent idler bandwidth at the L band.

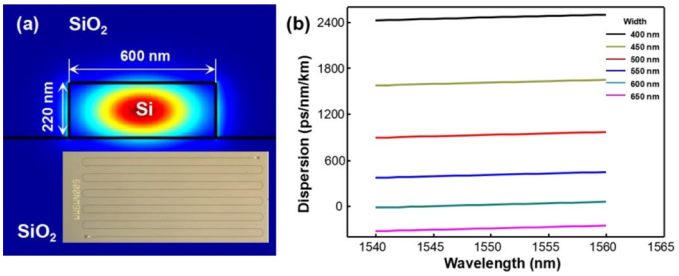

Fig. 5. (a) Schematic of cross-sectional layout of a silicon waveguide. Inset: top-view micrograph of a fabricated silicon waveguide. (b) Calculated group velocity dispersion as a function of wavelength for a range of waveguide widths. Copyright 2019, IEEE Xplore [55].

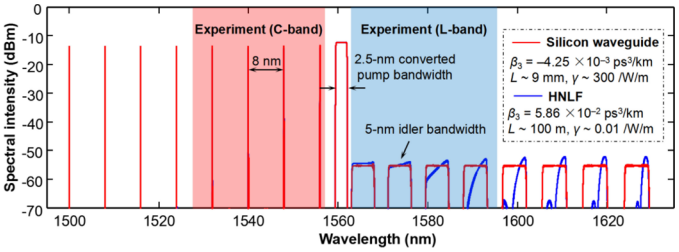

Fig. 6. Simulated FWM spectrum of the silicon waveguide (red line) and HNLF (blue line) for a 2.5-nm converted pump bandwidth, with the signal tuned from 1500 to 1556 nm. The red and blue shaded area represent the available experimental tuning range. Inset: parameters for the silicon waveguide and HNLF in the simulation. Copyright 2019, IEEE Xplore [55].

III. Advanced Temporal Imaging System With Dispersion Engineering

Based on the dispersion-engineered time-lens, the temporal aberration can be largely reduced, and the temporal NA will be expanded, thus the performance of temporal imaging systems can be significantly improved. In this section, our recent work about advanced temporal imaging system is presented in details, including the aberration-free time magnifier, large-temporal-NA PASTA, and aberration-free PASTA.

A. *Aberration-free time magnifier*

For an in-focus time magnifier, the main aberration comes from the TOD in the dispersive path for input and pump [32]. To construct a low-aberration time magnifier with long

recording length, the combination of DCF and LEAF was used to achieve large linear dispersion (fourth and higher-order dispersion neglected). As shown in the experimental setup in Fig. 7(a), both the input dispersion and the pump dispersion were provided by combining DCF and LEAF. In the current system, the SUT was dispersed for 35 ps^2 before being combined with the pump through the wavelength-division multiplexer (WDM). In the lower branch of the system, a broadband mode-locked laser (MLL) went through a dispersion of 71.2 ps^2 and was then pre-amplified by a low-noise erbium-doped fiber amplifier (EDFA). The following band-pass filter selected the spectral component from 1555 to 1565 nm, which is subsequently amplified again to 100 mW to generate the pump for the time magnifier. The pump and SUT are launched together into the HNLF, and the generated idler was filtered out and went through the output dispersion (2152.5 ps^2), which was then amplified again to became the final output of the time magnifier. Overall, the system satisfied the imaging condition [16]

$$\frac{-1}{\Phi_1''}+\frac{-1}{\Phi_2''}=\frac{-1}{\Phi_f''} \tag{7}$$

where the Φ''_1 (35 ps^2), Φ''_2 (2152.5 ps^2) and Φ''_f (35.6 ps^2) are the input output, and focal group-delay dispersions, respectively while the minus sign originates from the phase conjugation during the chosen parametric process. Therefore, the temporal magnification ratio is 61.5.

To characterize the performance of the time magnifier, a femtosecond pulse with 10 nm bandwidth and center wavelength of 1543 nm was used as input of the system. As shown in Fig. 7(b), in the FWM spectrum after the HNLF, a narrow-band idler was generated, which was then filtered out and became the temporally magnified signal after output dispersion. The femtosecond pulse is shifted temporally across 300 ps input window (input time scanning) and the corresponding output waveform was recorded.

As shown in Fig. 7(c), the output time is linearly proportional to the input time with a slope of 61.5. Moreover, thanks to the TOD elimination, the output pulse width during input time scanning is stable at 54 ps. The corresponding output pulse shape indicates negligible aberration from TOD. This feature is most critical for implementing the temporal scanning microscope, as ideally the overlapping areas should be identical in neighboring measurement frames so as to be clearly identified for image stitching. The small fluctuating tail of the waveform results from the impulse response of the photodetector, which is shown in the inset. On the basis of the results above, the average measured pulse width is 54 ps/61.5 = 878 fs. Since the real pulse width of the input signal is measured to be 470 fs through auto-correlation, the deconvolved impulse response or the temporal resolution of the time magnifier is calculated to be 740 fs. Therefore, the low-aberration time magnifier achieves a large TBWP of 300 ps/740 fs = 405.4 enabled by the large linear dispersion links in the system, which is comparable to the largest TBWP previously demonstrated in temporal imaging systems [33]. To demonstrate the output consistency, a group of ten system responses which corresponded to ten temporally shifted input pulses across the recording window were plotted as Fig. 7 (d) shows.

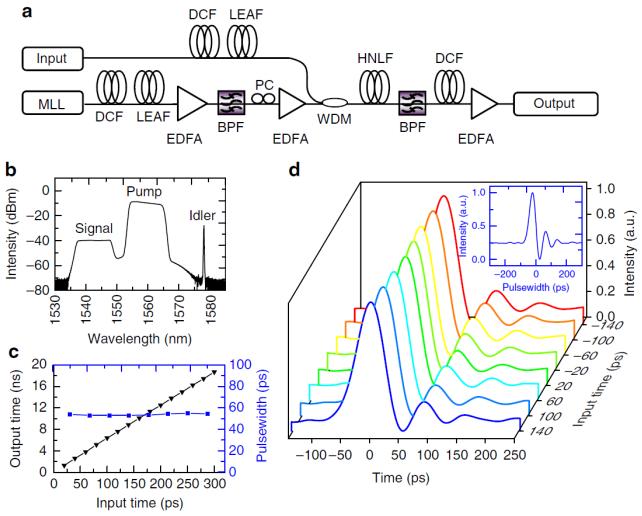

Fig. 7. Schematic representation and performance of the low-aberration time magnifier. (a) Experimental setup. (b) The optical spectrum after the HNLF when measuring a 470-fs pulse. (c) The output time (black, left axis) and pulse width (blue, right axis) of the time magnifier as a function of the input time. (d) The normalized output waveforms of the system when the input pulse is temporally shifted across the recording window. The corresponding output waveforms at each input time are labelled by a different colour. (inset). Copyright 2017, Springer Nature [39].

B. *Aberration-free PASTA*

Except for the combination of DCF and LEAF, another approach is an OPC-based, TOD compensation scheme, with accumulated β_2 and eliminated β_3. The setup consisted of SMF and DCF to provide opposite GVD and TOD, and HNLF was used to achieve OPC with parametric process, which was shown in Fig. 8. Sole DCF was applied as the comparison. In our experiments, OPC was firstly demonstrated to eliminate TOD and achieved a ±3400-ps^2 pure temporal dispersion of over 30-nm bandwidth. Leveraging this pure temporal dispersion, up to 2% of temporal aberrations were eliminated.

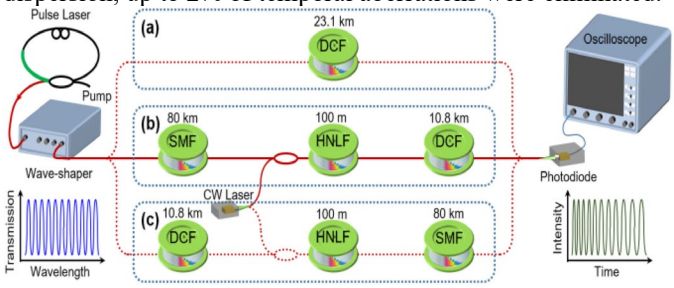

Fig. 8. Schematic diagram of the group delay dispersion measurement. (a) The normal dispersion is provided by 23.1-km DCF, with third-order dispersion. (b) The normal dispersion without third-order dispersion is provided by the OPC with 80-km SMF and 10.8-km DCF. (c) The anomalous dispersion without third-order dispersion is provided by the identical fibers with reversed position. Copyright 2021, IEEE Xplore [54].

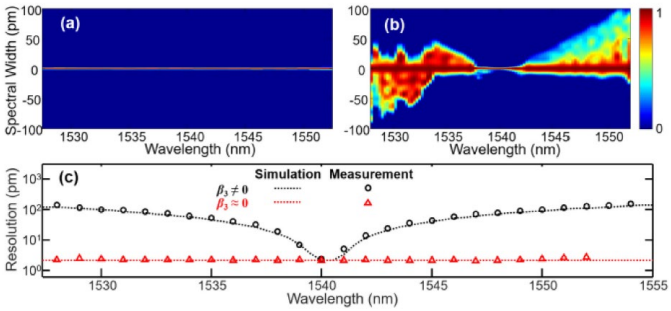

Fig. 9. Resolution improvement of the PASTA system with pure temporal dispersion. By tuning the signal under test from 1528 nm to 1552 nm, the measured spectral width in correspondence to the resolution is shown in (a) with pure temporal dispersion, and (b) with third-order dispersion. (c) The simulated (dotted line) and measured (black circle and red triangle) resolution degradations are figured out. Copyright 2021, IEEE Xplore [54].

PASTA system [46], [47] has been demonstrated as a flexible tool in single-shot spectrum measurements, especially for ultrafast non repetitive phenomena with arbitrary waveforms [34]. In pervious works, the resolution of the PASTA system was observed to be degraded, as it is away from the central wavelength, owing to the third-order dispersion in the output dispersion. Therefore, its wavelength observation bandwidth is usually constrained within 5 nm to 10 nm, as shown in Fig. 9(b). Here, the minimum 2-pm resolution (corresponds to 2.96-ps pulse width) was obtained at central 1540 nm by an asynchronous optical sampling (ASOPS) system [35],and it degraded to 15-pm as the wavelength shifted 2 nm to 1538 nm or 1542 nm, matched well with the simulation result (black dotted line) in Fig. 9(c). As Fig. 9(c) shows, after replacing the DCF with the pure temporal dispersion as the output dispersion, the wavelength induced spectral broadening was totally removed and 2-pm resolution was achieved for entire observation bandwidth (1527 - 1557 nm). Leveraging this pure temporal dispersion, the temporal focusing based PASTA system achieved the record ERP of 15000 (2000 in the case of real-time acquisition with 33-GHz bandwidth), the spectral broadening effect of the PASTA system was almost removed, and the observation bandwidth was enlarged to 30 nm.

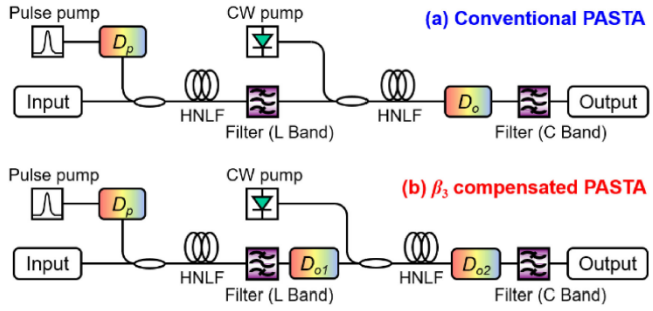

Fig. 10. Configuration of the PASTA system. (a) In the conventional PASTA system, the second-stage CW-pumped FWM is acted an optical phase conjugator, thus both the output dispersion (D_o) and the pump dispersion (D_p) can use identical type of DCF, which has large dispersion-to-loss ratio; (b) to compensate the higher-order dispersion of the output dispersion, it has been separated as two dispersive fiber D_{o1} (SMF) and D_{o2} (DCF), before and after the second-stage FWM. The other part of the configuration keeps identical. Copyright 2021, IEEE Xplore [54].

C. *Large-Temporal-NA PASTA*

Conventional PASTA system utilizes the HNLF as the parametric medium. However, the dispersion and dispersion slope of HNLF limits the spectral resolution as well as the observation bandwidth. To overcome such an inherent restriction, a dispersion-engineered waveguide, instead of the HNLF, was designed and fabricated to have a shorter interaction length in PASTA systems. Compared to conventional HNLF-based PASTA, the temporal NA of the silicon-based PATSA was enhanced by 2.5 times. Besides, a 1.3-pm spectral resolution and a 21-nm observation bandwidth are achieved thanks to its broadband phase-matching conditions. Finally, a waveguide paves the way to integrate the fiber-based system to more compact and portable devices.

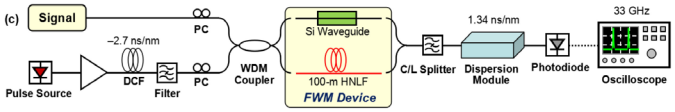

Fig. 11. Experimental setup of PASTA system. Copyright 2019, IEEE Xplore [55].

The experimental setup of PASTA is illustrated in Fig. 11. Two different nonlinear media are utilized for comparison: 9-mm silicon waveguide and 100-m standard HNLF, while the residual components of two scheme are completely identical. The output pulsed pump train has a repetition rate of 20 MHz and was temporally stretched by a –2.7-ns/nm DCF. The frequency chirp pumps were then amplified and filtered by a 2.5-nm band-pass filter. The generated swept pumps at the center wavelength $\lambda = 1560.8$ nm were combined with the input signals through a WDM coupler before undergoing FWM in either the silicon waveguide or the HNLF. The average input power to the tapered fiber before the silicon waveguide was 15.0 dBm for the pump and 13.0 dBm for the signal. At these powers, the impact of free carriers was negligible [36] and only the Kerr nonlinearity was considered. Meanwhile, both the pump and signal were aligned to the TE mode of the silicon waveguide. The coupling power was maintained to ensure fiber-to-chip alignment stability. Identical power levels were applied to the HNLF. After parametric process, the generated idler in the L-band was isolated using a C/L band splitter and then amplified using an L-band erbium-doped fiber amplifier. After the converging time-lens, the corresponding idler passed through a dispersion module (~1.34 ns/nm) to achieve aberration-free compressed pulses in focus of the temporal axis, which were detected by a 40-GHz photodiode and recorded by a 33-GHz real-time oscilloscope. In this experiment, the configuration was kept identical in the HNLF case for ease of comparison between the results.

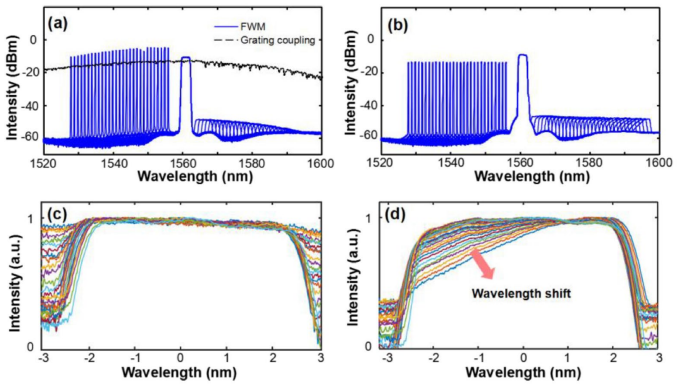

Fig. 12. Wideband pumped FWM. (a) FWM spectra after the silicon waveguide (blue line) and transmission spectrum of the grating coupling (black dashed line). (b) FWM spectra after the HNLF. (c)(d) Accumulated aligned idler spectra of (a) and (b), respectively. Copyright 2019, IEEE Xplore [55].

To better visualize the degrading of HNLF and the enhancement of the waveguide in terms of the conversion bandwidth, FWM spectra and their accumulated aligned idler spectra were measured and plotted in Fig. 12. When the signal wavelength was tuned from 1528 to 1556 nm, the desired idler shifts in the L band accordingly. Because of the grating coupling of the silicon waveguide, its transmission spectrum was not flat and had a particular spectral window, as indicated by the black line in Fig. 12(a). Consequently, the signal and idler spectra of the silicon waveguide also aligned with this envelope, and the overall parametric mixing spectra was almost flat by subtracting the signal and idler spectra with this envelope. In contrast, without the transmission loss of the coupling grating, the FWM spectrum of the HNLF was almost flat, and a higher conversion efficiency was also achieved, as shown in Fig. 12(b). However, their effective conversion bandwidths were different: for the silicon waveguide, the idler spectra were almost identical, twice the pump bandwidth (Fig. 12(c)), and the 2.5-nm bandwidth pump is fully converted to the 28-nm idler wavelength range. For the HNLF case, the shape of the idler spectrum distorted as it shifted to longer wavelengths (Fig. 12(d)), and the 2.5-nm bandwidth pump can only be fully converted to an idler wavelength range less than 10 nm. The FWM asymmetry mainly came from the dispersion-induced phase mismatching in the long HNLF [37]. Therefore, by implementing the time-lens based on the silicon waveguide, the limited converted pump bandwidth can be overcome, enlarging the temporal NA and improving the resolution of the PASTA system.

IV. Applications

Apart from the aforementioned temporal imaging systems based on time-lens, dispersion engineering has also thoroughly demonstrated its essentiality and exhibited its promising prospects through diverse applications including the ultrafast imaging and measurements. In this section, TOD elimination and its effect in multiple systems are included and discussed.

A. Panoramic-reconstruction temporal imaging (PARTI)

Combined with the aforementioned aberration-free time magnifier, single-shot real-time characterization with sub-picosecond resolution and nanosecond recording length has been feasible for investigating various ultrafast optical dynamics. The mechanism and temporal magnification part have been discussed in Section III. To demonstrate its capability of recording-length enhancement and dynamics observation, a period difference between the buffered replicas and the pump pulses was introduced, and the time magnifier captured a different section of SUT consecutively on each replica. In this way, a long SUT can be fully scanned in multiple steps and the complete waveform can be reconstructed from the magnified waveform of each stroboscopic acquisition. The experimental details of implementation are shown in Fig. 13.

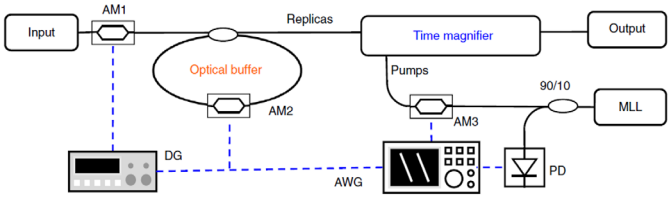

Fig. 13. Simplified experimental setup of the PARTI system, emphasizing key components for electronic synchronization. Copyright 2017, Springer Nature [39].

The key electronics can be divided into the following three groups. First of all, a repetition-rate-stabilized femtosecond fibre MLL and a 1.2 GHz photodetector together generated a 250 MHz electrical clock signal, which served as the time base of the whole system. Secondly, an arbitrary waveform generator (AWG), and a delay generator created electrical patterns that controlled the stroboscopic acquisition. Finally, the three AMs converted the electrical patterns to the optical domain, controlling the SUT loading (AM1), optical buffer switching (AM2) and time-magnifier-pump generation (AM3), respectively. More details of the system configuration can be traced in [39].

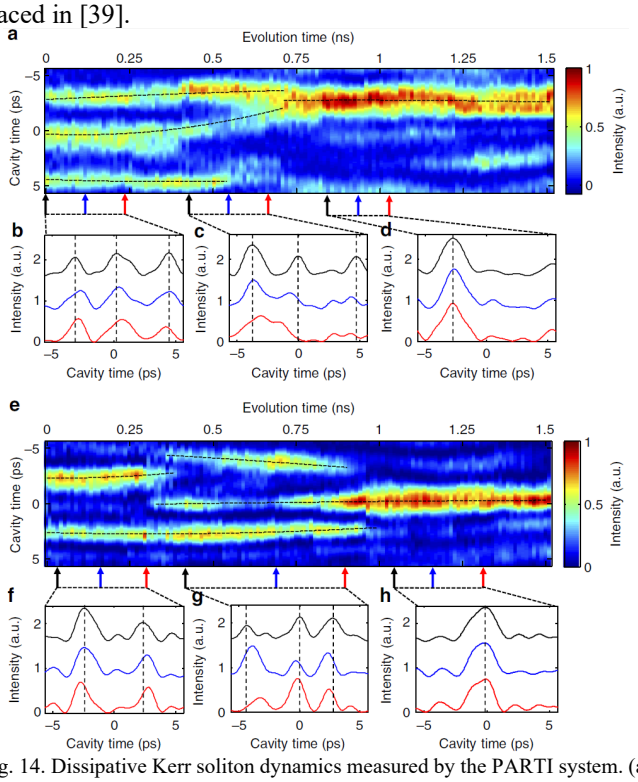

Fig. 14. Dissipative Kerr soliton dynamics measured by the PARTI system. (a) An example of 2D evolution portrait, depicting soliton fusion dynamics and transition from a triplet soliton state to a singlet soliton state. (b)-(d) Measured waveforms at different evolution time slices in each stage, illustrating stable

triplet solitons at the beginning stage (b), soliton fusion at the middle stage (c) and stable singlet soliton in the final stage (d). (e) Another example of 2D evolution portrait, showing an evolution from doublet solitons to triplet solitons and eventually to a singlet soliton. (f)–(h) Measured waveforms at different evolution time slices in each stage, illustrating soliton repulsion at the beginning stage (f), soliton attraction at the middle stage (g) and the stable singlet soliton at the final stage (h). For (a) and (e), black dashed curves emphasizing the soliton transition traces are plotted against the 2D portrait. Copyright 2017, Springer Nature [39].

Finally, to demonstrate the capabilities of the PARTI system, the system was applied to observe the dynamic evolution of dissipative Kerr solitons inside an ultrahigh-Q microresonator. Two sections of 1.5-ns-long waveform with a 740-fs resolution were reconstructed, which represent a TBWP of more than 2000. To clearly visualize the evolution details, we sectioned the one-dimensional waveform according to the cavity roundtrip time (11.29 ps) of the microresonator to rearrange the data into a 2D matrix and created 2D evolution portraits to depict the dissipative Kerr soliton transition dynamics.

In the first case, a transition process that resembled the simulation result in Fig. 14(a) was observed. As shown in Fig. 14(a), at the beginning stage (0 to ~400 ps), three solitons (triplet state) with almost equal intensity exist in the cavity. Fig. 14(b) plots the waveforms at three different time slices of 0 ps (black), 113 ps (blue) and 237 ps (red), which shows that the triplet solitons roughly maintain their intensities and positions in the cavity throughout the beginning stage. The three curves were vertically offset for clarity and vertical black dashed lines are plotted according to the soliton positions at 0 ps (black curve) to emphasize the position change of solitons at different time slices. After that, in the middle stage (400 to ~800 ps), the first two solitons start to become attracted to each other and eventually merge into a singlet soliton at ~800 ps. The third soliton is also shifted upwards during the merging of the other two solitons. However, the third soliton does not survive during the transition and starts to fade after 500 ps. The soliton fusion details are shown in Fig. 14(c), where waveforms at 440, 565 and 677 ps are shown. At these three specific time positions, the separation between the first two solitons evolves from 3.8 to 3 ps and then to 1.5 ps. After this transitioning middle stage, a singlet soliton state is achieved inside the cavity, and the state remains for more than 600 ps, or 53 cavity roundtrips. Similarly, three waveforms in this stage are shown in Fig. 14(d), indicating the high stability during the final stage. Black dashed curves emphasizing the soliton transition traces are plotted against the 2D portrait in Fig. 14(a) and (e), which are obtained by polynomials fitting the peak positions of the solitons.

In addition to the first example, a different dynamic process is also observed generating the singlet soliton state eventually but without soliton fusion. As shown in Fig. 14(e), in the first stage (0 to ~370 ps) two solitons co-exist in the cavity. In the meantime, the doublet solitons repulse each other slightly and the first soliton gradually fades away. At ~370 ps, the upper soliton disappears, but at the same time two other solitons emerge. In the second stage (370 ps – 1 ns), in contrast to the first stage, the triplet solitons are attracted to the centre slowly. At the end of the second stage, both the top and bottom solitons fade away, while the middle one survives and evolves into a singlet soliton with higher intensity in the final stage (1–1.5 ns). Similar to the first example, the singlet soliton state is much more stable compared to previous states and lasts over 500 ns. Again, waveforms at three different time slices are plotted together for each distinct stage, which shows weak pulse repulsion (f), weak pulse attraction (g) and stable single soliton state (h).

B. Aberration-free STEAM

Leveraging large temporal dispersion, time-stretch microscopy can acquire the spectral information and achieved an ultrahigh imaging framerate (~MHz). However, the existence of TOD will induce nonlinearity in dispersion, thus, there will be nonlinear frequency-to-time mapping and misalignment, which results in aberrations for the time-stretch microscopy [40]. Our OPC-based dispersion was directly applied in the time-stretch microscopy application. In our experiment, the standard test targets were used to quantify the aberrations. Here, the spatial disperser of the time-stretch microscopy (space-to-frequency mapping) was configured identical as in [38], and it achieved the spectral resolution of 0.18 nm and the corresponding spatial resolution of 2.3 μm. The deviation of the quasi-linear space-to-frequency mapping process was also measured by pulse delay methods, and it is observed from Fig. 15(a) that up to 15-μm spatial deviation is observed from the central to the edge of the spectral band. This deviation is only observable in the horizontal direction, while the vertical direction acquired by the translation stages is almost linear, as discussed in Fig. 15(c). To enhance the contrast of the minor spatial deviation, the images of the time-stretch microscopy with/without the third-order dispersion in different colors were overlapped, and their misalignment manifests the imaging aberrations as shown in Figs. 15(b)-(d). This aberration is similar when the test objects were rotated at different angles. To calibrate this aberration, digitally re-sampling the output time axis is the most straightforward way in post processing in electrical domain, while the OPC scheme introduced in this paper provides an alternative optical solution in optical domain.

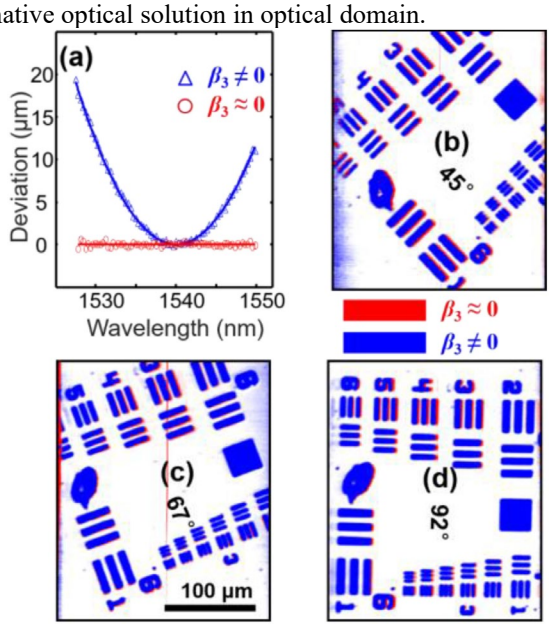

Fig. 15. Aberration observation of the time-stretch microscopy with/without the third-order dispersion. (a) The deviation of the quasi-linear space-to-frequency mapping process, and it is mainly from the third-order dispersion ($\beta_3 \neq 0$). (b)-(d) The resolution test target (USAF 1951, Group 6 and 7) was introduced

as the imaging object of the time-stretch microscopy, and rotated at different angle (45°, 67°, and 92°). Here, the blue and red colors represent the uncompensated and compensated third-order dispersion (β_3), respectively. Copyright 2021, IEEE Xplore [54].

C. Calibration-free OCT

The dispersive time stretch of the ultrashort pulse provides an inertia-free swept source without mechanical moving parts, and enables time-stretch OCT (TS-OCT) with a tens of MHz frame rate, which is determined by the repetition rate of the pulse source [41], [42]. The coherence length is proportional to the amount of dispersion, and a 25 mm imaging range has been realized [41]. While high-order dispersion (mainly third-order dispersion) exists in the dispersive fiber, the frequency-to-time mapping becomes nonlinear, which results in the spectral broadening in the Fourier domain and rapid degradation of the resolution and sensitivity as the imaging depth increases. Although the digital calibration [51] has solved this problem successfully, it takes up the majority time of the data processing (up to ~100 μs range), which is not the limiting factor for those conventional SS-OCT with a slow frame rate [kilohertz (kHz) range]. However, it makes TS-OCT challenging for realtime imaging subject to its MHz A-scan rate [43]. To achieve calibration-free OCT, a dispersion module, which consisted of DCF, and nonzero dispersion-shifted fiber (DSF) was used as the dispersion component of TS-OCT, which is shown in Fig. 16. By adjusting the length ratio of DCF and DSF, almost complete elimination of the third-order dispersion over a 40 nm bandwidth is achieved without sacrificing the second-order dispersion. Compared with the conventional TS-OCT, the acquired raw data can directly perform the Fourier transform, and the data processing time is greatly reduced by 82%. Moreover, a factor of 2.6 improvement in sensitivity roll-off (6.91 mm/dB) and a 14.2% increase in imaging depth (16 mm) at a 19 MHz sweep rate is realized in this calibration-free TS-OCT, which is shown in Fig. 17. It is significant for a large-scale real-time imaging, and the results of 2D in vivo biological tissue imaging have also been demonstrated the improvement.

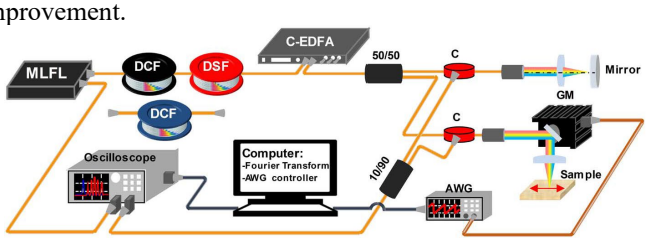

Fig. 16. Experimental setup of the TS-OCT with higher order dispersion compensation. C-EDFA, conventional band erbium-doped fiber amplifier; C, circulator; PD, photodetector; GM, galvo mirror. Copyright 2019, Optical Society of America [23].

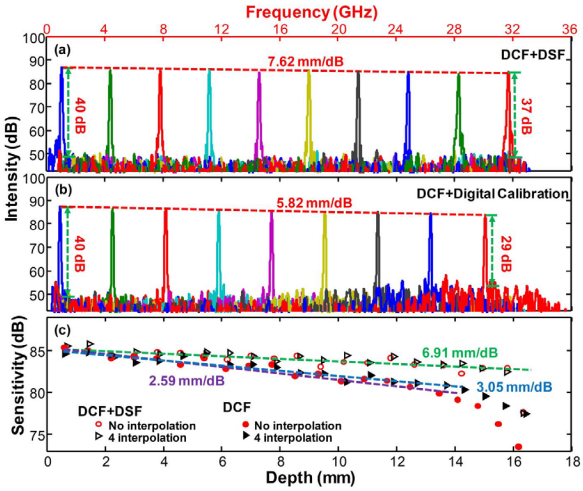

Fig. 17. PSF roll-off performance of the TS-OCT (a) with or (b) without higher order dispersion compensation; (c) sensitivity roll-off performance of the TS-OCT with different interpolations. Dashed lines of different colors are linear fits to experimental data under difference interpolation. Green (DSF+DCF with 0 and 4 interpolation); blue and purple (DCF + digital calibration with 0 and 4 interpolation). Copyright 2019, Optical Society of America [23].

D. Terahertz Analyzer

Apart from the above-mentioned optical spectrum analyzer, a novel ultrafast radio-frequency (RF) spectrum measurement was developed as well, named frequency-domain light intensity spectrum analyzer (f-LISA), which has achieved a high frame rate of 94 MHz [44].

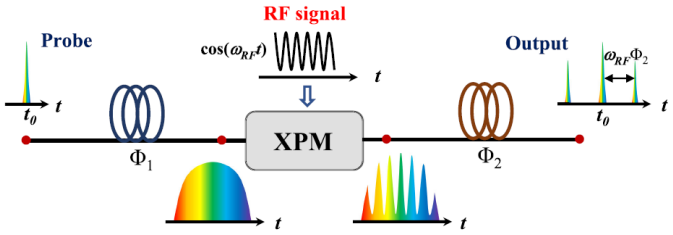

Fig. 18. Schematic of f-LISA, Φ_1 and Φ_2 represent the front and output dispersion of f-LISA, respectively. XPM represents the cross-phase modulation to modulate the RF signal into the probe. Copyright 2022, IEEE Xplore [52].

Figure 18 shows the schematic of f-LISA which consists of three parts: the front dispersion medium, the nonlinear medium, and the output dispersion medium. Firstly, the probe spectrum is mapped into time domain through the front dispersion Φ_1. Subsequently, the intensity of SUT with radio frequency ω_{RF} is modulated to the phase of the stretched probe through XPM in nonlinear medium. Then the spectrum of RF signal carried by the probe is injected into the output dispersion medium to achieve frequency-to-time mapping. Finally, the RF spectrum information is directly recorded in the time domain. However, the previous work has only considered the second-order dispersion and omitted the influence of the TOD in the mapping process, which leaves an optimizing space for the parameters including bandwidth and resolution.

In order to achieve a pure second-order dispersion, the OPC method which included SMF, phase conjugation part and DCF as discussed in Section II was used to reduce the output TOD. More details of the OPC method and the experimental setup can be found at [52].

To characterize the enhancement induced by the dispersion optimization, the bandwidth is characterized by tuning the input RF signal from 100 GHz to 2.3 THz. Due to the working range of the optical amplifier, the bandwidth of optimized f-LISA is up to 2.2 THz, as shown in Fig. 19(a). Moreover, the slight uptrend may be caused by the unevenness of the optical amplifier. In contrast, due to the pulse broadening and mapping distortion induced by the output TOD, the pulse intensity of original f-LISA decreases rapidly with the increasing radio frequency and the 3-dB bandwidth degrades to 0.825 THz as shown in Fig. 19(b).

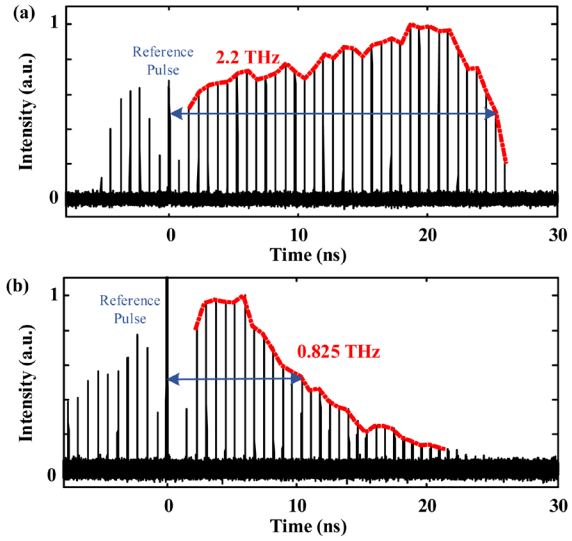

Fig. 19. (a), (b). The bandwidth of the optimized and original f-LISA. Copyright 2022, IEEE Xplore [52].

E. *Ultrafast Swept Source*

Last but not least, we proposed and experimentally demonstrated a new type of ultrafast discrete swept source based on two chirped optical frequency combs (OFCs) with different repetition rates [52]. The frequency sweeping is implemented by the Vernier effect between the two OFCs rather than any inertial filtering component. Figure 20(a) explained the principle for generating a discrete swept source though FWM between two chirped OFCs. The two combs with repetition rates of f and $f + \Delta f$ were time stretched before serving as the signal and pump, respectively. Throughout the text, two pulses with the same index from the two combs can be called the nearest neighbors. Time delay between the m-th nearest neighbors is $\Delta t_m = m \cdot \Delta f / f^2$, which discretely increases in step of $\delta t = \Delta f / f^2$. As shown in Fig. 20(b), when the chirping rate of the signal pulses is twice that of the pump pulses, a quasi-continuous and frequency sweeping idler pulse train will be generated. The time delay between the nearest neighbors is proportionally converted to the frequency shift of the corresponding idler pulse. Finally, Fig. 20(c) gives the frequency-to-time mapping relation of the generated swept source. Here, the dispersion of time stretch is implemented by the combination of DCF and LEAF, with total dispersion of about 0.31 ns/nm. The fiber lengths of the DCF and LEAF are carefully designed so that a linear dispersion is achieved, with the TOD compensated.

To characterize the system performance, different swept rates from 10 kHz to 129 kHz, 329 kHz, 857 kHz, and 1.03 MHz are demonstrated by simply changing the repetition rate difference between the two OFCs, as is shown in Fig. 21. The wavelength step is proportional to the swept rate and calculated to be about 3.8 pm at 10-kHz. Simultaneously, the instantaneous linewidth is estimated to be about 0.03 nm using the roll-off performance of the point spread functions, as is shown in Fig. 22. High linearity (R2 = 0.999998) frequency sweeping is verified by extracting the phase of the interference signal, which has demonstrated its robust roll-off performance.

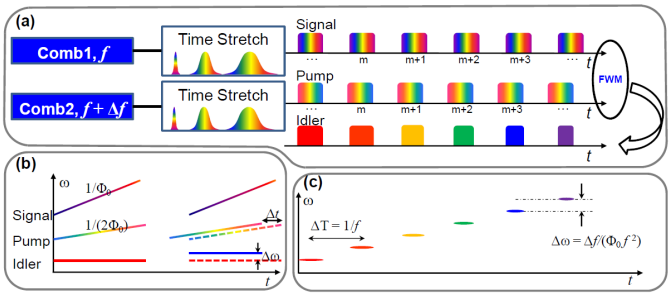

Fig. 20. (a) The principle of the proposed ultrafast swept source. (b) The frequency-to-time mapping relation of the FWM process. (c) Frequency versus time of the output swept source. Copyright 2019, Optical Society of America [53].

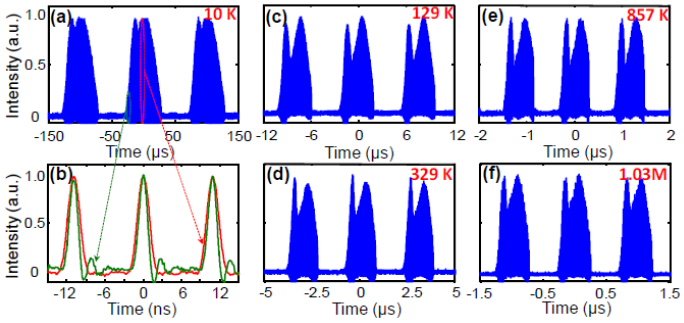

Fig. 21. (a) Temporal waveform of the swept source at 10 kHz and (b) its zoom-in observations. (c-f) Temporal waveforms of the swept source at different swept rates. Copyright 2019, Optical Society of America [53].

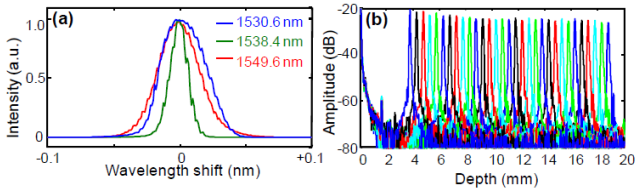

Fig. 22. (a) Static linewidth at different wavelength measured by OSA. (b) The PSFs measured by an interferometer. Copyright 2019, Optical Society of America [53].

V. Conclusion

In this paper, we review our recent efforts about dispersion engineering for multiple temporal imaging modalities based on the time-lens. Specifically, TOD elimination has been adopted in two approaches, different fiber of reverse dispersion combinations and the OPC-based compensation schemes. Both have been leveraged in various implementations and verified their feasibility to achieve better performance. In temporal magnification system, the recording length of time magnifier has been extended to 1.5 ns thanks to absence of third-order dispersion on the signal path. Therefore, transient dynamics of Kerr solitons are thoroughly captured. In OCT, third-order

dispersion is compensated so that the mapping between wavelength and time is linear to simplify the calibration process. OPC-based third-order compensation scheme is applied in PASTA and STEAM. Besides, highly-nonlinear waveguide instead of nonlinear fiber is designed and fabricated to have less third-order dispersion and flat second-order dispersion so that the temporal NA of PASTA has been enhanced by 2.5 times. Finally, dispersion optimizations have also been leveraged on the Terahertz analyzer and the ultrafast swept sources to achieve more feasibility on optical generations and waveform characterizations. We hope those efforts could enlighten more innovative implementations of dispersion engineering in temporal imaging modalities in the future.

REFERENCES

[1] R. Ulbricht, E. Hendry, J. Shan, T. F. Heinz, and M. Bonn, "Carrier dynamics in semiconductors studied with time-resolved terahertz spectroscopy," Reviews of Modern Physics, vol. 83, no. 2, pp. 543, 2011.

[2] M. Breusing, C. Ropers, and T. Elsaesser, "Ultrafast carrier dynamics in graphite," Physical Review Letters, vol. 102, no. 8, pp. 086809, 2009.

[3] G. Herink, B. Jalali, C. Ropers, and D. R. Solli, "Resolving the build-up of femtosecond mode-locking with single-shot spectroscopy at 90 MHz frame rate," Nature Photonics, vol. 10, no. 5, pp. 321-326, 2016.

[4] S. H. Yun et al., "Comprehensive volumetric optical microscopy in vivo," Nature Medicine, vol. 12, no. 12, pp. 1429-1433, 2006.

[5] W. Wieser, B. R. Biedermann, T. Klein, C. M. Eigenwillig, and R. Huber, "Multi-megahertz OCT: High quality 3D imaging at 20 million A-scans and 4.5 GVoxels per second," Optics Express, vol. 18, no. 14, pp. 14685-14704, 2010.

[6] J. Hodgkinson and R. P. Tatam, "Optical gas sensing: a review," Measurement science and technology, vol. 24, no. 1, p. 012004, 2012.

[7] B. Bernhardt et al., "Cavity-enhanced dual-comb spectroscopy," Nature Photonics, vol. 4, no. 1, pp. 55-57, 2010.

[8] T. Herr et al., "Temporal solitons in optical microresonators," Nature Photonics, vol. 8, no. 2, pp. 145-152, 2014.

[9] S. T. Cundiff, J. M. Soto-Crespo, and N. Akhmediev, "Experimental evidence for soliton explosions," Physical Review Letters, vol. 88, no. 7, pp. 073903, 2002.

[10] A. F. Runge, N. G. Broderick, and M. Erkintalo, "Observation of soliton explosions in a passively mode-locked fiber laser," Optica, vol. 2, no. 1, pp. 36-39, 2015.

[11] M. H. Frosz, O. Bang, and A. Bjarklev, "Soliton collision and Raman gain regimes in continuous-wave pumped supercontinuum generation," Optics Express, vol. 14, no. 20, pp. 9391-9407, 2006.

[12] B. H. Kolner, "Space-time duality and the theory of temporal imaging," IEEE Journal of Quantum Electronics, vol. 30, no. 8, pp. 1951-1963, 1994.

[13] G. Patera, D. B. Horoshko, and M. I. Kolobov, "Space-time duality and quantum temporal imaging," Physical Review A, vol. 98, no. 5, pp. 053815, 2018.

[14] R. Salem, M. A. Foster, and A. L. Gaeta, "Application of space–time duality to ultrahigh-speed optical signal processing," Advances in Optics and Photonics, vol. 5, no. 3, pp. 274-317, 2013.

[15] B. H. Kolner and M. Nazarathy, "Temporal imaging with a time lens," Optics Letters, vol. 14, no. 12, pp. 630-632, 1989.

[16] C. V. Bennett and B. H. Kolner, "Principles of parametric temporal imaging. I. System configurations," IEEE Journal of Quantum Electronics, vol. 36, no. 4, pp. 430-437, 2000.

[17] C. V. Bennett and B. H. Kolner, "Principles of parametric temporal imaging. II. System performance," IEEE Journal of Quantum Electronics, vol. 36, no. 6, pp. 649-655, 2000.

[18] O. Aso, M. Tadakuma, and S. Namiki, "Four-wave mixing in optical fibers and its applications," dEp, vol. 1, no. 2, 1999.

[19] M. Cronin-Golomb, B. Fischer, J. White, and A. Yariv, "Theory and applications of four-wave mixing in photorefractive media," IEEE Journal of Quantum Electronics, vol. 20, no. 1, pp. 12-30, 1984.

[20] M. Arumugam, "Optical fiber communication—An overview," Pramana, vol. 57, no. 5, pp. 849-869, 2001.

[21] D. Tosi, "Review of chirped fiber Bragg grating (CFBG) fiber-optic sensors and their applications," Sensors, vol. 18, no. 7, pp. 2147, 2018.

[22] H. Kaushal and G. Kaddoum, "Optical communication in space: Challenges and mitigation techniques," IEEE Communications Surveys & Tutorials, vol. 19, no. 1, pp. 57-96, 2016.

[23] L. Zhang, L. Chen, Z. Lei, Y. Duan, C. Zhang, and X. Zhang, "Calibration-free time-stretch optical coherence tomography with large imaging depth," Optics Letters, vol. 44, no. 17, pp. 4135-4138, 2019.

[24] M. E. Marhic, Fiber optical parametric amplifiers, oscillators and related devices. Cambridge university press, 2008.

[25] T. Okuno, M. Hirano, T. Kato, M. Shigematsu, and M. Onishi, "Highly nonlinear and perfectly dispersion-flattened fibres for efficient optical signal processing applications," Electronics Letters, vol. 39, no. 13, pp. 1, 2003.

[26] M. Lillieholm, M. Galili, L. Grüner-Nielsen, and L. K. Oxenløwe, "Detailed characterization of CW-and pulsed-pump four-wave mixing in highly nonlinear fibers," Optics Letters, vol. 41, no. 21, pp. 4887-4890, 2016.

[27] M. Karlsson, "Four-wave mixing in fibers with randomly varying zero-dispersion wavelength," JOSA B, vol. 15, no. 8, pp. 2269-2275, 1998.

[28] A. Tikan, S. Bielawski, C. Szwaj, S. Randoux, and P. Suret, "Single-shot measurement of phase and amplitude by using a heterodyne time-lens system and ultrafast digital time-holography," Nature Photonics, vol. 12, no. 4, pp. 228-234, 2018.

[29] J. T. Mok, J. L. Blows, and B. J. Eggleton, "Investigation of group delay ripple distorted signals transmitted through all-optical 2R regenerators," Optics Express, vol. 12, no. 19, pp. 4411-4422, 2004.

[30] E. Dulkeith, F. Xia, L. Schares, W. M. Green, and Y. A. Vlasov, "Group index and group velocity dispersion in silicon-on-insulator photonic wires," Optics Express, vol. 14, no. 9, pp. 3853-3863, 2006.

[31] M. Dinu, F. Quochi, and H. Garcia, "Third-order nonlinearities in silicon at telecom wavelengths," Applied Physics Letters, vol. 82, no. 18, pp. 2954-2956, 2003.

[32] C. V. Bennett and B. H. Kolner, "Aberrations in temporal imaging," IEEE Journal of Quantum Electronics, vol. 37, no. 1, pp. 20-32, 2001.

[33] M. A. Foster, R. Salem, D. F. Geraghty, A. C. Turner-Foster, M. Lipson, and A. L. Gaeta, "Silicon-chip-based ultrafast optical oscilloscope," Nature, vol. 456, no. 7218, pp. 81-84, 2008.

[34] C. Zhang, B. Li, and K. K.-Y. Wong, "Ultrafast spectroscopy based on temporal focusing and its applications," IEEE Journal of Selected Topics in Quantum Electronics, vol. 22, no. 3, pp. 295-306, 2015.

[35] P. A. Elzinga, F. E. Lytle, Y. Jian, G. B. King, and N. M. Laurendeau, "Pump/probe spectroscopy by asynchronous optical sampling," Applied Spectroscopy, vol. 41, no. 1, pp. 2-4, 1987.

[36] Q. Lin, O. J. Painter, and G. P. Agrawal, "Nonlinear optical phenomena in silicon waveguides: modeling and applications," Optics Express, vol. 15, no. 25, pp. 16604-16644, 2007.

[37] C. Zhang, K. K. Cheung, P. Chui, K. K. Tsia, and K. K. Y. Wong, "Fiber-optical parametric amplifier with high-speed swept pump," IEEE Photonics Technology Letters, vol. 23, no. 14, pp. 1022-1024, 2011.

[38] X. Dong et al., "Ultrafast time-stretch microscopy based on dual-comb asynchronous optical sampling," Optics Letters, vol. 43, no. 9, pp. 2118-2121, 2018.

[39] B. Li, S.-W. Huang, Y. Li, C. W. Wong, and K. K. Y. Wong, "Panoramic-reconstruction temporal imaging for seamless measurements of slowly-evolved femtosecond pulse dynamics," Nature Communications, vol. 8, no. 1, pp. 61, 2017.

[40] K. Goda, K. K. Tsia, and B. Jalali, "Serial time-encoded amplified imaging for real-time observation of fast dynamic phenomena," Nature, vol. 458, no. 7242, pp. 1145-1149, 2009.

[41] J. Xu, C. Zhang, J. Xu, K. K. Y. Wong, and K. K. Tsia, "Megahertz all-optical swept-source optical coherence tomography based on broadband amplified optical time-stretch," Optics Letters, vol. 39, no. 3, pp. 622-625, 2014.

[42] J. Kang, P. Feng, X. Wei, E. Y. Lam, K. K. Tsia, and K. K. Y. Wong, "102-nm, 44.5-MHz inertial-free swept source by mode-locked fiber laser and time stretch technique for optical coherence tomography," Optics Express, vol. 26, no. 4, pp. 4370-4381, 2018.

[43] C. M. Eigenwillig, B. R. Biedermann, G. Palte, and R. Huber, "K-space linear Fourier domain mode locked laser and applications for optical coherence tomography," Optics Express, vol. 16, no. 12, pp. 8916-8937, 2008.

[44] L. Chen, Y. Duan, C. Zhang, and X. Zhang, "Frequency-domain light intensity spectrum analyzer based on temporal convolution," Optics Letters, vol. 42, no. 14, pp. 2726-2729.
[45] G. P. Agrawal, "Nonlinear fiber optics," in Nonlinear Science at the Dawn of the 21st Century: Springer, 2000, pp. 195-211.
[46] C. Zhang, J. Xu, P. Chui, and K. K. Y. Wong, "Parametric spectro-temporal analyzer (PASTA) for real-time optical spectrum observation," Scientific Reports, vol. 3, no. 1, pp. 1-6, 2013.
[47] C. Zhang, X. Wei, and K. K. Y. Wong, "Performance of parametric spectro-temporal analyzer (PASTA)," Optics Express, vol. 21, no. 26, pp. 32111-32122, 2013.
[48] F. Begum et al., "Novel broadband dispersion compensating photonic crystal fibers: Applications in high-speed transmission systems," Optics & Laser Technology, vol. 41, no. 6, pp. 679-686, 2009.
[49] L. Gruner-Nielsen et al., "Dispersion-compensating fibers," Journal of Lightwave Technology, vol. 23, no. 11, pp. 3566-3579, 2005.
[50] R. N. Bracewell and R. N. Bracewell, The Fourier transform and its applications. McGraw-Hill New York, 1986.
[51] X. Yu, X. Liu, S. Chen, Y. Luo, X. Wang, and L. Liu, "High-resolution extended source optical coherence tomography," Optics Express, vol. 23, no. 20, pp. 26399-26413, 2015.
[52] R. Wang, L. Chen, N. Yang, Y. Du, C. Zhang, and X. Zhang, "Performance Improvement of Frequency-Domain Light Intensity Spectrum Analyzer (f-LISA)," Journal of Lightwave Technology, vol. 40, no. 14, pp. 4663-4673, 2022.
[53] Y. Duan, X. Dong, L. Zhang, Y. Li, Z. Lei, L. Chen, X. Zhou, C. Zhang, and X. Zhang, “Ultrafast discrete swept source based on dual chirped combs for microscopic imaging,” Optics Express, vol. 27, no. 3, pp. 2621-2631, 2019.
[54] L. Chen, X. Dong, N. Yang, L. Zhang, Z. Lei, C. Zhang and X. Zhang, “Pure Temporal Dispersion for Aberration Free Ultrafast Time-Stretch Applications,” Journal of Lightwave Technology, vol. 39, no. 17, pp. 5589-5597, 2021.
[55] H. Zhou, N. Yang, G. Liu, L. Chen, Y. Wang, C. Zhang, K. K. Y. Wong and X. Zhang, “Large-Temporal-Numerical-Aperture Parametric Spectro-Temporal Analyzer Based on Silicon Waveguide,” IEEE Photonics Journal, vol. 11, no. 5, pp. 1-10, 2019.